Bone diagenesis and origin of calcium phosphate nodules from a hominid site in the Lukeino Formation (Tugen Hills, Kenya)

Perrine Dericquebourg, Alain Person, Loïc Ségalen, Martin Pickford, Brigitte Senut, Nathalie Fagel

Bone diagenesis and origin of calcium phosphate nodules from a hominid site in the Lukeino Formation (Tugen Hills, Kenya)

Perrine Dericquebourg (1), Alain Person (2), Loïc Ségalen (2), Martin Pickford (3), Brigitte Senut (3), Nathalie Fagel (1)

(1) Université de Liège. Laboratoire AGEs (Argile, Géochimie et Environnements sédimentaires), UR Géologie. Quartier Agora. Allée du six Août 14, B-4000 Liège, Belgique.
(2) Sorbonne Université, CNRS-INSU, Institut des Sciences de la Terre Paris, ISTeP UMR 7193, F-75005 Paris, France.
(3) CR2P UMR 7207 - MNHN, CNRS, Sorbonne Université, Muséum National d'Histoire Naturelle, Département « Origines et évolution », CP 38, 8 rue Buffon, 75231 Paris Cedex 05.

Corresponding authors: Perrine.Dericquebourg@alumni.uliege.be & Loïc Ségalen (loic.segalen@sorbonne-universite.fr)

Highlights:

• Calcium phosphate nodules retrieved in the Upper Miocene sedimentary sequence (Lukeino Fm)
• The nodules are composed of a francolite matrix with no internal structure.
• The diagenesis is related to an advanced degree of bone transformation induced by physical and chemical processes, and possibly bacterial activity.
• The process occurred in a relatively dry and confined environment such as a lake edge or marsh.

Abstract:

The Lukeino Formation (6.09-5.68 Ma; Kenya) is a fossiliferous fluvio-lacustrine sedimentary sequence (~100 m thick), which yielded the fossil remains of the oldest East African bipedal hominid, called *Orrorin tugenensis*. At one of the hominid sites (Aragai), centimetric to pluri-centimetric, indurated calcium phosphate nodules occur in a specific sedimentary layer. Mineralogical and geochemical analyses, coupled with SEM, optical microscopy and cathodoluminescence observations, were performed on four calcium phosphate nodules and one bone showing differential alteration, with characteristics locally similar to that of the nodules, in order to determine the nature and origin of these nodules. A crystallinity index (CI) and histological index (HI) were also assigned to these samples to characterize their degree of transformation. Analyses reveal that all nodules and the studied bone have a similar mineralogical and chemical composition. Nodules show no internal structure and are composed of a carbonate-fluorapatite matrix, including feldspars, clays and spheres of iron and manganese oxides. Their high CI indicates significant recrystallization compared to modern bone. The altered bone shows infilling of the trabecular cavities, characterized by a clay deposit along the walls, oxide spheres with a silica center and carbonate-fluorapatite baguettes. In the highly altered area of the bone, a phenomenon of dissolution and dismantlement of bone structures adjacent to an area characterized by the presence of a phosphate matrix is observed. The genesis of these calcium phosphate nodules seems to result from an advanced stage of transformation of bones, due to a combination of physical, chemical and biological (bacterial) processes. The different stages of diagenesis are characterized by the incorporation of components from the sedimentary layer (including diatoms) and by neoformations of clays and oxides in the bone pores. The bone structure is affected by fracturing and dissolution of carbonate-hydroxylapatite, which reprecipitated in bone cavities under the form of carbonate-fluorapatite automorphic crystals. Then, the bone

structures and mineral neoformations were affected by a dismantlement phenomenon, which increased the dissolution of the bone apatite. This resulted in a carbonate-fluorapatite matrix, in which no trace of the initial bone structure is visible. This particular mechanism of genesis of calcium phosphate nodules most probably takes place by action of fluid circulation in a confined environment such as a lake edge or marsh.

Keywords: Bone structure dissolution, phosphate matrix, carbonate-fluorapatite neoformation, mineralogy, fluvio-lacustrine environment, Upper Miocene, Lukeino Formation.

1. Introduction

The Lukeino Formation is a fluvio-lacustrine sedimentary sequence about 100 m thick, which crops out in the Tugen Hills (Kenya) (Pickford, 1974; Pickford et al., 2009). Radiometric dates (K-Ar) performed on the Kabarnet Trachyte underlying the formation and on the Kaparaina Basalts overlying it indicate an age of 6.09±0.18 (2σ) Ma and 5.68±0.14 (2σ) Ma, respectively (Sawada et al., 2002). Sedimentary deposits associated with Palaeolake Lukeino are mainly silty clay to sandy clay, with a volcanic ash component, and locally include diatomite layers, ferruginous layers, lacustrine phosphorite and carbonate horizons (Dericquebourg et al., 2015; Dericquebourg, 2016).

This sedimentary formation is richly fossiliferous and in particular contains many fossils belonging to large vertebrates (Pickford, 1974; Pickford et al., 2009). The Lukeino Formation is also known to have yielded the remains of the oldest East African bipedal hominid, named *Orrorin tugenensis* (Senut et al., 2001; Pickford et al., 2002). At Aragai, which is one of the late Miocene sites that yielded hominid remains (Pickford and Senut, 2001; Senut et al., 2018), a specific sedimentary layer contains pluri-centimetric calcium phosphate nodules. These nodules have a different habitus compared to the phosphate horizons previously identified in the Lukeino Formation, and they appear to have a distinct origin. Some fossils sampled at this site also show a particular alteration and have characteristics similar to the nodules.

Geochemical and mineralogical analyses, as well as optical microscopy, scanning electron microscope (SEM) and cathodoluminescence observations, were performed on these nodules and bone fragments. The aim of this study is to characterize the nature of the calcium phosphate nodules and to identify the mechanisms responsible for their genesis, in relation to palaeoenvironmental conditions.

2. Geological context

The upper Miocene sediments of the Lukeino Formation crop out in the Eastern foothills of the Tugen Hills, northwest of Lake Baringo, in the Kenyan part of the East African Rift (Pickford, 1974, 1978) (Fig. 1). The area corresponds to a large tilted block within the rift (Pickford, 1974; Chapman et al., 1978; Hill et al., 1986; Pickford et al., 2009). It is located between the Elgeyo Escarpment, which forms the western flank of the rift and the axial rift depression in which Lake Baringo and Lake Bogoria are located.

This part of the Kenyan Rift has been subjected to intense volcanic and tectonic activity since the early Miocene. The formation of half-grabens has structured the region and led to the uplift of the nascent Tugen Hills during the Middle Miocene, favouring the development of a series of graben lakes (Pickford, 1974; Hill et al., 1986; Williams and Chapman, 1986; Tiercelin et al., 1987; Tiercelin and Lezzar, 2002). Between 7 and 6.1 Ma, volcanic activity was characterized by the eruption of extensive lavas of the Kabarnet Trachyte Formation. At the same time, faults located in the Tugen Hills were reactivated, leading to the creation of a new graben about 6.5 Ma, called the Lukeino Depression in which Palaeolake Lukeino and perilacustrine flats developed. Fluvio-lacustrine deposits (~100 m thick), mainly silty-clay to sandy-clay, with diatomites locally, carbonates and phosphate layers (Dericquebourg, 2016) (Fig. 2a), accumulated in this depression from about 6.1 to 5.7 Ma ago. Sediment deposition was interrupted by several volcanic eruptions, leading to the accumulation of ash layers, a basaltic flow (Kapsomin Basalt) and a dolerite sill (Rormuch Sill). The Lukeino Formation was sealed by the Kaparaina Basalts that infilled the depression and obliterated the palaeolake.

Radiometric dates (K-Ar) on the lava flows (measured on groundmass) that bracket the Lukeino Formation, indicate an age between 6.09 ± 0.14 (2σ) Ma for the underlying Kabarnet Trachyte, and 5.68 ± 0.18 (2σ) Ma for the overlying Kaparaina Basalts at the top of

111 the series (Sawada et al., 2002). Other studies performed on these lava flows indicated similar
112 ages: between 6.06 ± 0.13 Ma (2σ; sanidine; Hill et al., 1985) and 6.37 ± 0.05 Ma (1σ;
113 anorthoclase; Kingston et al., 2002) for the Kabarnet Trachyte, and between 5.65 ± 0.13 Ma
114 (2σ; feldspar; Hill et al., 1985) and 5.72 ± 0.05 Ma (1σ, anorthoclase; Deino et al., 2002) for
115 the Kaparaina Basalt.

116 The studied material comes from the site of Aragai, located at the southwest end of
117 Palaeolake Lukeino. Sedimentary deposits at this site (~40 m thick) overlie the Kabarnet
118 Trachyte and underlie the Rormuch Sill (Fig. 2a). They are located stratigraphically in the
119 lower half of the Lukeino Formation. The sediments are composed of silty-clay alternating
120 with coarser deposits, sandy-clay (Dericquebourg, 2016). The deposits are intercalated with
121 several argillized volcanic ash horizons. Diatomite layers of significant thickness are also
122 observed in the upper half of the sequence. These volcano-sedimentary and biogenic
123 sediments contain unstable components (e.g., volcanic glasses) rich in Si, Fe and Mn. These
124 elements will be rapidly released by weathering and hydrothermal alteration (alkaline rift
125 lakes with pH greater than 10, Tiercelin and Vincens, 1987). They are then transported in
126 solution by the sedimentary pore fluids to matrix surrounding the bones (see Trueman et al.,
127 2006). In the alkaline rift lakes, Eh is a reducing agent controlled by the degradation of bone
128 organic matter and pH ± 10 controlled by the dissolution of biophosphate (Pfretzschner,
129 2004).

130

131 **3. Materials**

132 Nineteen samples of powder extracted from four nodules and one altered bone from
133 Aragai were analysed (Table 1). An additional powder sample extracted from a well-
134 preserved bone from a nearby site (Kapcheberek) was analysed for comparison. Samples were
135 collected in 2004 as part of the Kenya Palaeontology Expedition.

All nodules came from a single sedimentary horizon (ARG 13) located approximately 4.5 m above the Kabarnet Trachyte (Fig. 2a), at the base of the Aragai sedimentary sequence. This weakly consolidated sedimentary layer with a thickness of about 20 cm is clayey, red in colour, and includes many pluri-centimetric nodules (Fig. 2b).

These highly indurated and massive nodules show neither internal structure nor porosity at the macroscopic scale and present some colour variations (from light grey to red-brown) observed in fresh sections. The choice of powder sampling areas was based on these colour differences to identify any changes in the mineralogical or chemical composition (Fig. 2c). Six samples were collected on the largest (~10 cm in diameter) nodule (labeled NR). It shows some variations in terms of colour (Fig. 2c): the top part of the nodules is bright red (sample NR01) to lighter red (sample NR02); the median part of the nodule is red-brown in colour (sample NR03) with slightly lighter areas (sample NR04); the lower part of the nodule area is the lightest, between light brown-pinkish (sample NR05) and light grey-pink (sample NR06). The NG nodule is smaller (~4 cm in diameter) and lighter. The three samples collected correspond to the three colours observed on this nodule (light grey for the sample NG01; pink for NG02; dark grey for NG03) (Fig. 2c). Four samples were taken on the NM nodule with a diameter of ~6 cm with colours ranging from light grey-pinkish (samples NM01 and NM02) to dark brown (sample NM03). Sample NM04 corresponds to a pinkish area observed on the side (Fig. 2c). The smallest nodule PNR (~3 cm in diameter) has a homogeneous bright red internal colour. Two powder samples were collected (PNR01 and PNR02) respectively at the center of the nodule and in the peripheral area (Fig. 2c).

In addition, four samples were collected on a relatively large altered bone (OS; lengh:10 cm; width: 5 cm ; thickness: 4 cm). This bone likely corresponds to a metaphysis fragment of a long bone belonging to a large unidentified mammal (Fig. 2c). The bone fragment is characterized by a generally well preserved trabecular structure, with some

crystals (length: ~100/180µm; width: 25/30 µm) visible on the walls of cavities in the bone (sample OS01). In the central part of the bone, the trabecular structures are clearly identifiable but a red infilling is locally observed in the cavities of the trabecular bone (sample OS03). The OS02 sample was collected in a red, highly altered area with unidentified bone structures. This bone area shows characteristics similar to the nodules. A last sample (OS04) was collected in the cortical peripheral area (under the former periosteal surface), which seems relatively well preserved.

An additional powder sample (KAP07) was extracted from an epiphysis (~6 cm in diameter) of long bone belonging to a large unidentified mammal. The bone, showing low taphonomic transformation, is considered to be an unaltered bone and was analysed for comparison with the OS altered bone and nodules. This bone fragment comes from the Kapcheberek site, about 2.5 km northwest of Aragai, and located stratigraphically in the Kapcheberek Member according to the denomination of Sawada et al. (2002) (Fig. 2a).

4. Methods

The four calcium phosphate nodules and the two bone fragments were cut in half through their transverse plane using a diamond water saw. The powder samples (n=20; Fig. 2c) were collected on the fresh sections using a rotary drill equipped with a diamond tip. Samples were extracted from different areas to study the variations of mineralogy, crystallinity and chemical composition. All analyses were carried out at the Biomineralizations and Sedimentary Environments Laboratory (BES)-ISTeP of Sorbonne University (Paris), except SEM observations made at the Petrology, Geochemistry, Magmatic Mineralogy Laboratory (PG2M)-ISTeP (Sorbonne University, Paris).

All samples were analysed by X-ray diffraction (XRD) using the powder method. The ARG 13 sedimentary horizon (Figure 2) which yielded the nodules was also analysed.

Samples were manually crushed in an agate mortar to obtain a fine (10 microns) powder. The analyses were conducted with a SIEMENS D501 diffractometer. The apparatus is equipped with a 2θ device and a copper anticathode tube (30 kv, 10 mA) to a wavelength of λCuKα = 1.5418 Å. All samples were studied following the same protocol. The acquisition range of the diffractograms is between 3° and 72° 2θ with a step of 0.02° 2θ and a time per step of 1 s. Interpretations of the diffractograms were performed using the MacDiff software. The semi-quantitative estimation of the relative proportions of mineral species was derived from the calculation of the surfaces of the major peak for each mineral identified (Moore and Reynolds, 1997). Subsequently, a crystallinity index (CI) of the apatite was calculated from the XRD diffractogram of all analyzed samples, according to the method of Person et al. (1995)). - The CI corresponds to the sum of peak heights [112] at 2.784 Å, [300] at 2.709 Å and [202] at 2.629 Å, divided by the height of the major peak [211] at 2.801 Å. The CI value increases with the recrystallization degree of the apatite, and ranges generally between ~0, which corresponds to the carbonate-hydroxylapatite constituting a fresh bone, and ~1 for the highly recrystallized apatite, associated with a bone showing major taphonomic transformations. The variations on the CI calculations are ± 0.02.

Elemental geochemical analyses were performed on four samples from two nodules (NM01, NM03, NM04 and PNR01) and three samples from the OS bone (OS01, OS02, OS04). Sampling was conducted with a rotary drill equipped with a diamond-tipped burr. 50 mg of powder was dried overnight at 80 °C and weighed into a Teflon beaker before being digested in 5 ml of 30% nitric acid (Merck, suprapur) and heated at 80 °C for 1 h. The resulting solution was then diluted with deionized water to a total volume of 50 ml, stocked in polypropylene or Teflon tubes and kept for analysis; the standard used for calibration is the NIST SRM1400 “bone ash” following the protocol developed in Maurer et al., (2011).

The phosphorus percentage was determined by a UV Visible absorption spectrophotometer Spectronic 301 - MILTON ROY; fluorine dosing was carried out using a combined selective electrode of fluoride ions (DC219-F model of METTLER TOLEDO); barium, strontium, iron and manganese contents were determined by ICP-AES with a HORIBA JOBIN YVON JY2000 instrument. Calcium and magnesium were measured with flame atomic absorption spectrophotometer using a HITACHI Z-8100 device. The uncertainty of measurements is ± 5%.

Observations by optical microscopy were made on polished thin sections from the four nodules (NG, NM, NR and PNR) and the two bones (OS and KAP07) mainly to check the internal organization of nodules and the preservation of bone structures. The preservation of the bone microstructure is represented by the histological index (HI) defined by Hedges et al. (1995) according to the typology of Hackett (1981) to estimate the proportion of intact bone, based on the preservation of some features, such as the Haversian systems, the lamellar structures or osteocytes. The HI ranges between 0, for a sample having no recognizable structure, and 5, for a very well-preserved sample, almost indistinguishable from fresh bone. A HI was determined for each studied sample to assess the degree of taphonomic transformation. SEM observations were also made on thin sections of the NR and NG nodules and the OS bone, using a ZEISS supra V5 instrument provided with a BRUKER detector in energy dispersive spectroscopy (EDS). Additional observations by optical cathodoluminescence were performed on thin sections from the NR nodule and the OS bone, with an OPEA Catodine instrument. These analyses allow the study of the internal structures, the mineralogical composition of samples and the location of mineral neoformations.

5. Results

5.1. X-ray diffraction analyses

The ARG 13 clay layer containing nodules is composed of 90% smectite (Fig. 2d and Table 1) and of ~5% quartz and ~5% sanidine.

All of the nodules have a similar mineralogical composition. They are composed of 70-100% phosphate (Fig. 2e and Table 1). The phosphate mineral constituting these nodules is carbonate-fluorapatite (francolite), which is confirmed by elemental geochemistry analyses (Table 2). The other minerals observed are smectite (0-10%) and sanidine (~0-20%). Opal C-T (cristobalite-tridymite) was identified in only one sample from the NG nodule (NG02; ~10%) and iron and manganese oxides (goethite and groutite; 5-15%) were observed in 3 samples (NR04; NM02; NM03). Quartz identified in the enclosing clay layer is not observed in the nodules. There is no obvious link between a specific colour zone (redder or greyer zone) in the nodules and a particular mineralogy. The only noticeable change is a stronger occurrence of oxides in the browner areas (Table 1 and Fig. 2). All samples from the nodules have a high crystallinity index (CI), with relatively close values ranging between ~0.7 and 0.9 (Table 1 and Fig. 3). NG and NM nodules have a CI mean value (~0.76) similar to NR and PNR nodules (~0.83). -

The apatite proportion in the OS bone ranges between 70% in the highly altered red area (sample OS02) and 100% in the well preserved cortical area (OS04) (Table 1). The other minerals identified in some areas of bone are smectite (OS02; ~10%), quartz (OS02 and OS03; ~10%), sanidine (OS02; ~15%) and goethite and/or groutite (OS01 and OS03; 10-25%). The crystallinity index is highly variable from one sample to another within this bone, between ~0.6 and 1.3 (Table 1 and Fig. 3). The lowest CI is associated with the peripheral cortical area (OS04; Fig. 2c). The area showing a red filling with visible bone structures has a very high CI of ~0.9 (sample OS03). The two highest values of the CI are associated respectively with the well-preserved trabecular area but with crystals observed on the bone walls (OS01; ~1) and to the red area, with bone structure highly destructured which is similar

to the nodules (OS02; ~1.3). The high CI are related to a high proportion of recrystallized apatite expressed in trabecular porosity as hexagonal crystals corresponding to two processes: a major dissolution of carbonate-hydroxylapatite and the neoformation of carbonate-fluorapatite. The well-preserved bone KAP07, analysed for comparison, is composed of 100% apatite and its CI is ~0.4, substantially lower compared to the other samples (Table 1 and Fig. 3).

5.2. Geochemical analyses

Geochemical analyses were performed on three samples from the NM nodule and one sample from the PNR nodule. The P_2O_5 content in the samples ranges between 30% and ~33% (Table 2a); the percentage of CaO is 42-46% and the fluorine content is between 2.5% and 3%. The CaO/P_2O_5 and F/P_2O_5 ratios are respectively of 1.4 and 0.1 for all samples, and are identical with the values of the carbonate-fluorapatite reference (Table 2c; francolite mineral from Wheal Franco, Devon, England; Palache et al., 1951). Nodules also contain low proportions of MgO (0.01-0.03%), SrO (0.5-0.7%), BaO (0.03-0.07%) and MnO (0.3-0.7%). The Fe_2O_3 values are slightly more scattered than the other elements (Fig. 4), ranging from ~2% (NM01 and PNR01) to 5% for the NM03 sample. For this last sample, XRD analysis reveals the presence of goethite and/or groutite (~15%; Table 1) in a dark area from the NM nodule. Moreover the proportions of Fe_2O_3 in the samples are high compared to the carbonate-fluorapatite reference.

The contents of P_2O_5 (32-35%), CaO (43-48%) and F (2-3%) of the three analysed samples from the OS altered bone are relatively constant and in the range of values of results obtained on nodules (Table 2a and Fig. 4). The CaO/P_2O_5 (1.3-1.4) and F/P_2O_5 (0.1) ratios are also identical to the values obtained on the nodules and indicate that the chemical composition

of this bone is closer to the carbonate-fluorapatite than to the carbonate-hydroxylapatite (corresponding to the SRM; Table 2b), which constitutes a fresh bone (Table 2a and b and Fig. 4). As for the nodules, BaO (0.03-0.04%), MgO (0.01-0.02%), SrO (0.3%), MnO (0.2-0.4%) and Fe_2O_3 (1-2%) are included in relatively constant proportions in the chemical composition of samples from the OS bone.

5.3. Optical microscopy, SEM and cathodoluminescence observations

All nodules show the same characteristics in terms of mineralogy and lack of internal structure. They are composed of a phosphate micritic matrix (Fig. 5a and b). The EDS analyses indicate that the matrix is comprised of carbonate-fluorapatite, which appears bright yellow (Baele et al., 2011) on the images obtained by cathodoluminescence observations (Fig. 5a). Similar luminescence patterns have been recorded for dentine coming from fossil Gomphotheriidae and Hippopotamidae teeth collected in the Lukeino Formation (Ségalen et al., 2008). This matrix includes a few crystals of K-feldspar (sanidine) (Fig. 5a), as well as clays and many spheres composed of iron and manganese oxides (~10-30 μm; Fig. 5c) with a center of silica (identified by EDS analysis). Diatom fragments are also observed by SEM, locally in the NG nodule. They are not clearly identifiable but some preserved characters suggest that they could possibly belong to the genus *Aulacoseira*. SEM observations locally show an irregular porosity in the apatite matrix, of about ~100-300 μm (Fig. 5b). Crystals of carbonate-fluorapatite, as needles, are observed at the transition between these cavities and the apatite matrix (Fig. 5c). No bone structure, as defined by Hedges et al. (1995), was observed in these four nodules. The values of HI for nodules are therefore equal to 0 (Table 1 and Fig. 3).

The analysis of the OS bone reveals significant variability in the preservation of structures. The cortical peripheral area (OS04) is well-preserved, with a 4<HI<5 (Table 1 and

311 Fig. 3). The bone structures are also particularly well-preserved in the trabecular area
312 corresponding to sample OS01 (HI = 4). In the areas of samples OS02 and OS03,
313 observations by optical microscopy show that the bone structures (trabecular area) are highly
314 altered to almost non-existent. For these samples, the value of HI is between 0 and 1.

315 In well-preserved trabecular areas, mineral neoformations were observed in all bone
316 cavities. Fig. 6 shows the succession of these neoformations, which develop inside a studied
317 cavity (Fig. 6a, b and c). A clay deposit is observed along the walls of a cavity in the
318 trabecular bone structure (Fig. 6a and c). Observations by optical microscopy show the
319 presence of oxide spheres (diameter of ~100 μm) in significant quantities inside the cavity
320 (Fig. 6b). SEM observations coupled with EDS analysis confirm the presence of iron and
321 manganese oxides, located above the clay deposits (Fig. 6a). The center of these oxide
322 spheres is composed of silica (Fig. 6a and c). Toward the center of the bone cavity,
323 rectangular-shaped crystals of carbonate-fluorapatite grow above the spheres of oxides and
324 agglomerate together to form an apatite matrix (Fig. 6a and b). These neoformations partially
325 fill the cavities of the trabecular bone structure, reducing the porosity (Fig. 6c). The
326 arrangement of these automorphic crystals of carbonate-fluorapatite in the trabecular structure
327 of bone (Fig. 6d) is revealed by cathodoluminescence observations (bright yellow crystals).
328 Although in this area of the OS bone, the trabecular structures, composed of carbonate-
329 hydroxylapatite, are well-preserved, they show local alteration visible by optical microscopy
330 (Fig. 6b; area with a yellow colour). The altered apatite corresponds to darker areas observed
331 by SEM and cathodoluminescence (Fig. 6a and d). SEM observations also indicate the
332 presence, in the cavity of the trabecular bone structure, of a few fragments of unidentifiable
333 diatoms (~1-10μm).

334 The left upper part of the bone (samples OS02 and OS03, figure 2c) corresponds to a
335 highly altered area with total or partial disappearance of the bone structures with a red

infilling, similar to the nodules. SEM observations evidence an unsystematic arrangement of the remaining bone apatite (Fig. 7). Two cavities of the trabecular bone are clearly visible and are partially filled by clay neoformations, oxide and carbonate-fluorapatite automorphic crystals toward the center. However, the trabecular structure surrounding the cavity is fractured and shows significant alteration. Fig. 7 shows that beyond these partially preserved cavities, the bone structures are unidentifiable, only fragments of bone apatite are observed in a matrix. This matrix is composed of francolite, corresponding to carbonate-fluorapatite crystals, which are amalgamated. The matrix also includes some oxide spheres with a centre of silica and clays. The remaining porosity is enclosed by baguettes (automorphic crystals) of francolite and oxide spheres, corresponding to a ghost of the bone cavity. This area corresponds to a transitional phase between well-preserved trabecular structures and the part of the OS bone showing a red infilling with a facies similar to that of the nodules, which illustrates the diagenetic transformation of bones.

In comparison, the trabecular bone structures are well-preserved, and no filling of cavities is observed in the KAP07 bone. A histological index of 4 is assigned to this bone (Table 1 and Fig. 3).

6. Discussion

6.1. Characterization of bones and calcium phosphate nodules

Nodules are composed of a carbonate-fluorapatite matrix including clays, oxides with a centre of silica, and sometimes feldspars or diatom fragments (Fig. 5 and Table 1). They show no internal structure and porosity is almost absent. In bone cavities, neoformations of clays, spheres of oxides with a centre of silica, and carbonate-fluorapatite baguettes develop along walls (Fig. 6 and Table 1). Nodules and the bone therefore contain the same mineral assemblage.

All nodules have a similar chemical composition (Table 2), except for an enrichment in iron linked to the presence of oxides observed locally. The chemical composition of the nodules is similar to the studied altered bone (Table 2 and Fig. 4). However, we note slightly higher FeO, MnO and MgO contents associated with the clays and oxides incorporation in the nodules compared to the bone. Their abundance in the OS bone also increases with the degree of alteration (Fig. 4 and Table 2).

The crystallinity index (CI) of the carbonate-fluorapatite is high for nodules suggesting pervasive recrystallization, and low for the well-preserved parts of the studied bones. The histological index (HI) is 0 for nodules and is relatively high for the well-preserved bones (Fig. 3). The high values of CI and HI of the OS bone (OS02 & OS03) are caused by the presence of the highly altered areas, which have values similar to the nodules. It is the presence of carbonate-fluorapatite (stable form: insoluble Pasteris and Ding, 2009), which is indistinguishable from carbonate-hydroxylapatite in the calculation of the CI by XRD, which causes the high values of CI. The carbonate-fluorapatite (francolite) is neoformed in the nodule. In some fossil bones, the carbonate-fluoroapatite is precipitated from the dissolution of a large part of the bone biomineral (carbonate-hydroxylapatite: bio-apatite) soluble in the intra-sediment solutions that circulate in the natural porosities of the fossil bones. The carbonate-hydroxylapatite gradually loses its **CO_3 radicals** and becomes less and less soluble (ie.Trueman et al., 2006; Pan and Darwell , 2010, Aufort et al., 2019).

All the analyses performed on these samples therefore indicate that the calcium phosphate nodules from Aragai have characteristics extremely similar to bone showing an advanced degree of diagenesis. The results would also suggest an evolution of the structures and mineral arrangement inside bones culminating in the formation of nodules.

6.2. Genesis of calcium phosphate nodules

SEM, optical microscopy and cathodoluminescence observations, performed on nodules and the bone from Aragai, allow the identification of the likely mechanisms responsible for bone alteration leading to the formation of calcium phosphate nodules. The increase in the degree of alteration of bones can be associated with an increase of the crystallinity index (CI) and a decrease of the histological index (HI). The first stages of bones diagenesis (early diagenesis) have been described in many studies (Garland, 1989; Hedges and Millard, 1995; Hedges, 2002; Jans et al., 2002; Trueman et al., 2006; Fernandez-Jalvo et al., 2010; Hinz and Kohn, 2010; Keenan, 2016; Keenan and Engel, 2017). A summary of these processes is shown in Fig. 8. Initially a fresh bone (Fig. 8a), characterized by a HI of 5 (Hedges et al., 1995) and a CI ~0 (Person et al., 1995), is subjected to microbial activity and collagen degradation (Pfretzschner, 2004; Kendall et al., 2018). The bone structure, particularly the Haversian canals and osteons, are then affected by micro-fracturing mechanisms (Fig. 8b). These stages of early diagenesis take place at pH of 8-10 (Pfretzschner, 2004) and reveal first *in situ* apatite recrystallization (Fig. 6-c, b – altered carbonate-hydroxylapatite and Fig. 8b). This corresponds to the disappearance of the biological structure on the edge of the bone fragments whose anatomic shapes are still preserved.

The subsequent stages of bone transformation, , are characterized by the precipitation of minerals in the bone cavities and the alteration of the bone structure. The mineral neoformations observed along the walls of trabecular cavities (Fig. 6) suggest that in the bone pores the clays accumulate first, together with components present in the environment, such as detrital feldspars or diatoms (Fig. 8c).

Neoformation of iron and manganese oxide spheres, with a centre of silica, corresponds to a second generation of minerals, which accumulate contiguously along the trabecular walls, on top of the clays (Fig. 6 and 8d). The silica in solution originates from the dissolution of diatoms and silica mobility in the trabecular cavities involves pH conditions

411 higher than 9 (Iler, 1979). The formation of spheres requires a reduction in pH. The Fe and
412 Mn mobility requires suboxic condiditons. Meanwhile, the fracturing of bone structures
413 continues and intensifies (due to the taphonomic processes and internal neoformations); the
414 carbonate-hydroxylapatite constituting the bone structures begins to dissolve (Fig. 6 and 8d).
415 Microscope observations reveal the presence of carbonate-fluorapatite automorphic crystals
416 inside the trabecular cavities. They seem to develop on top of clays and oxides spheres along
417 the walls (Fig. 6 and 8e). It is likely that the bone undergoes a process of dissolution of
418 carbonate-hydroxylapatite, which recrystallizes *in situ* in the form of carbonate-fluorapatite
419 automorphic crystals. However, this requires that fluoride is available in sufficient quantities
420 in the environment. Hydrothermal springs, the presence of which is recorded at some sites in
421 the Lukeino Formation (Pickford et al., 2009) could supply fluorine. This hypothesis is
422 discussed in the case of deposition of lacustrine phosphorite horizons in Dericquebourg et al.
423 (2015).

424 Observations on the OS bone clearly show that the bone structures, as well as mineral
425 neoformations in the cavities, are then affected by a diagenetic process (Fig. 7). The
426 phenomena of dissolution-reprecipitation of bone apatite increased and are associated with an
427 increase of fracturing of the trabecular structures (Fig. 8f). Carbonate-fluorapatite
428 automorphic crystals develop inside fractures and cavities, where they amalgamate to fill
429 them almost completely, and form a phosphate matrix (Fig. 7 and 8g). Fig. 7 illustrates the
430 dismantlement phenomenon of bones, characterized by a dispersion of the altered bone
431 fragments , clays and oxides, coupled with the formation of the carbonate-fluorapatite matrix,
432 which includes these components (Fig. 8h). This causes a gradual decrease of the porosity and
433 the disappearance of identifiable bone structures (Fig. 7 and 8i), and leads to the formation of
434 calcium phosphate nodules. Composed of a carbonate-fluorapatite matrix including oxides,
435 clays and locally feldspars (Fig. 5 and 8j), they are therefore characterized by the absence of

internal structure, with a HI equal to 0 (Fig. 3 and 5) and a high CI (Fig. 3) indicating a significant degree of transformation.

Mineralogical analyses of this clay layer (Fig. 2 and Table 1) and sedimentary context suggest a relatively poorly drained environment (Dericquebourg, 2016). The integration of diatom fragments and detrital particles from the environment (feldspar and clay) as well as the dismantlement processes of bone structures require fluid circulation. However, the dissolution of bone apatite and the carbonate-fluorapatite precipitation *in situ* in the bone cavities indicate a relatively confined environment. This suggests that these processes of bone diagenesis and genesis of these single calcium phosphate nodules probably took place in a lake edge or marshy environment.

7. Conclusion

The aim of this study was to characterize calcium phosphate nodules observed in a specific sediment layer of the Aragai sedimentary sequence, located at the base of the Lukeino Formation, and to determine their genesis. The mineralogical and geochemical analyses, coupled with observations by optical microscopy, SEM and cathodoluminescence, of four nodules and one bone, which shows differential alteration, highlighted several points:

1) Nodules are composed of a carbonate-fluorapatite matrix, including clays, feldspars, spheres of oxides with a centre of silica, and locally rare fragments of diatoms. They show no internal structure.
2) In the trabecular area of the studied bone, mineral neoformations of clays, oxide spheres with a centre of silica and carbonate-fluorapatite automorphic crystals develop inside cavities, filling them up. The most altered part of the bone shows characteristics similar to the nodules, with disappearance of osseous structures and formation of a carbonate-fluorapatite matrix.

3) The formation of nodules is related to mineral neoformations in the bone cavities and dissolution of carbonate-hydroxylapatite constituting the bone structures, which precipitates *in situ* in the form of carbonate-fluorapatite. These processes are coupled with a dismantlement phenomenon leading to the formation of an apatite matrix with extremely low porosity, and including the mineral neoformations.
4) The mineralogy of the sediment layer containing these calcium phosphate nodules indicates that the dismantlement processes, as well as the integration of diatoms, require fluid circulation and the *in situ* recrystallization suggests a confined environment taking place in a lake edge or marshy environment.

The genesis of the calcium phosphate nodules which occur at the base of the Lukeino Formation, is related to an advanced degree of bone transformation in a confined environment with suboxic phases and basic pH (similar to the modern lakes and hydrothermal circulations observed in the Gregory rift) which led to mobility of Fe, Mn elements and SiO_2, respectively.

Acknowledgements

Authorization to carry out research in the Tugen Hills was provided by the Government of Kenya (The Ministry of Research and Technology, at the time the Ministry of Higher Education, Science and Technology). Local affiliation is with the Orrorin Community Organisation. The field work was financed by the CNRS (GDRI 193, UMR 7207), the French Ministry of Foreign Affairs (Advisory Commission on Archaeological Research Abroad). The authors acknowledge Egerton University (Kenya), as well as the colleagues of the Kenya Palaeontology Expedition for their input on the field. We wish greatly to thank Omar Boudouma (ISTeP-Sorbonne Université) for the acquisition of SEM images; Marylène Person, Nathalie Labourdette and Jamel Benmamar (ISTeP-Sorbonne Université) for their help regarding respectively geochemical and XRD analyses; Frédéric Delbès (ISTeP-

Sorbonne Université) for producing the thin sections. Lastly we also acknowledge the three anonymous reviewers for their useful comments.

References

Aufort, J., Gervais, C., Ségalen, L., Labourdette, N., Coelho-Diogo, C., Baptiste, B., Beyssac, O., Amiot, R., Lécuyer, C., Balan, E., 2019. Atomic scale transformation of bone in controlled aqueous alteration experiments, Palaeogeography, Palaeoclimatology, Palaeoecology 526, 80-95.

Baele, J.-M., Papier, S., Barriquand, L., Barriquand J., 2011. Insights into the use of cathodoluminescence for bone taphonomy of fossil Ursidae from the Azé Cave, Saône-et Loire, France. Quaternaire, Hors-série 4, 291-296.

Chapman, G.R., Lippard, S.J., Martyn, J.E., 1978. The stratigraphy and structure of the Kamasia Range, Kenya Rift Valley. Journal of the Geological Society of London 135, 265-281.

Deino, A.L., Tauxe, L., Monaghan, M., Hill, A., 2002. $^{40}Ar/^{39}Ar$ geochronology and paleomagnetic stratigraphy of the Lukeino and lower Chemeron Formations at Tabarin and Kapcheberek, Tugen Hills, Kenya. Journal of Human Evolution 42, 117-140.

Dericquebourg, P., Person, A., Ségalen, L., Pickford, M., Senut, B., Fagel, N., 2015. Environmental significance of Upper Miocene phosphorites at hominid sites in the Lukeino Formation (Tugen Hills, Kenya). Sedimentary Geology 327, 43-54.

Dericquebourg, P., 2016. Les dépôts sédimentaires de la Formation de Lukeino, enregistreurs des fluctuations environnementales, associées aux premiers hominidés est-africains (Collines Tugen, Rift Gregory, Kenya), PhD Thesis, http://hdl.handle.net/2268/201893 Liège University.

510 Fernandez-Jalvo, Y., Andrews, P., Pesquero, D., Smith, C., Marin-Monfort, D., Sanchez, B.,
511 Geigl, E.-M., Alonso, A., 2010. Early bone diagenesis in temperate environments. Part I:
512 Surface features and histology. Palaeogeography, Palaeoclimatology, Palaeoecology 288,
513 62-81.
514 Garland, A.N., 1989. Microscopical analysis of fossil bone. Applied Geochemistry 4, 215-
515 229.
516 Hacket, C.J., 1981. Microscopical focal destructions (tunnels) in exhumed human bone.
517 Medicine, Science, and the Law 21, 243-265.
518 Hedges, R.E.M., 2002. Bone diagenesis: an overview of processes. Archaeometry 44, 319–
519 328.
520 Hedges, R.E.M., Millard, A.R., 1995. Bones and Groundwater: Towards the Modelling of
521 Diagenetic Processes. Journal of Archaeological Science 22, 155-164.
522 Hedges, R.E.M., Millard, A.R., Pike, A.W.G., 1995. Measurements and relationships of
523 diagenetic alteration of bone from three archaeological sites. Journal of Archaeological
524 Science 22, 201-209.
525 Hill, A., Drake, R., Tauxe, L., Monaghan, M., Barry, J.C., Behrensmeyer, A.K., Curtis, G.,
526 Jacobs, B.F., Jacobs, L.L., Johnson, N., Pilbeam, D., 1985. Neogene palaeontology and
527 geochronology of the Baringo Basin, Kenya. Journal of Human Evolution 14, 759 -773.
528 Hill, A., Curtis, G., Drake, R., 1986. Sedimentary stratigraphy of the Tugen Hills, Baringo,
529 Kenya. In: Frostick, L.E., Renaut, R.W., Reid, I., Tiercelin, J.-J. (Eds.), Sedimentation in
530 the African Rifts. Geological Society of London Special Publication 25, pp. 285-295.
531 Hinz, E.A., Kohn, M.J., 2010. The effect of tissue structure and soil chemistry on trace
532 element uptake in fossils. Geochimica et Cosmochimica Acta 74, 3213-3231.
533 Iler, R.K., 1979. The Chemistry of Silica: Solubility, Polymerization, Colloid and Surface
534 Properties and Biochemistry of Silica. Wiley (ed). 896p.

Jans, M. M. E., Kars, H., Nielsen-Marsh, C. M., Smith, C. I., Nord, A. G., Arthur, P., & Earl, **N., 2002**. In situ preservation of archaeological bone. A histological study within a multidisciplinary approach. Archaeometry 44, 343-352.

Keenan, S.W., 2016. From bone to fossil: a review of the diagenesis of bioapatite. American Mineralogist 101, 1943-1951.

Keenan, S.W., Summers Engel, A., 2017. Early diagenesis and recrystallization of bone. Geochimica et Cosmochimica Acta 196, 209-223.

Kendall, C., Høier Eriksen, A.-M., Kontopoulos, I., Collins, M.J., Turner-Walker, G., 2018. Diagenesis of archeological bone and tooth. Palaeogeography, Palaeoclimatology, Palaeoecology 491, 21-37.

Kingston, J.D., Jacobs, B.F., Hill, A., Deino, A., 2002. Stratigraphy, age and environments of the late Miocene Mpesida Beds, Tugen Hills, Kenya. Journal of Human Evolution 42, 95-116.

Maurer, A.-F., Gerard, M., Person, A., Barrientos, I., del Carmen Ruiz, P., Darras, V., Durlet, C., Zeitoun, V., Renard, M., Faugère, B., 2011. Intra-skeletal variability in trace elemental content of Precolumbian Chupicuaro human bones: the record of post-mortem alteration and a tool for palaeodietary reconstruction. Journal of Archaeological Science 38, 1784–1797.

Moore, D.M., Reynolds, R.C., 1997. X-Ray Diffraction and the Identification and Analysis of Clay Minerals (Second Edition). Oxford University Press, Oxford, 378pp.

Palache, C., Berman, H., Frondel, C., 1951. Dana's System of Mineralogy (Seventh Edition). John Wiley and Sons, INC, New York, 1124pp.

Pan, H., Darwell, B.W., 2010. Effect of carbonate on hydroxyapatite solubility. Crystal Growth & Design10, 845–850.

559 Pasteris J.D., Ying D.Y., 2009. Experimental fluoridation of nanocrystalline apatite.
560 American Mineralogist 94, 53-63.
561 Person, A., Bocherens, H., Saliège, J.-F., Paris, F., Zeitoun, V., Gérard, M., 1995. Early
562 diagenetic evolution of bone phosphate: An X-ray diffractometry analysis. Journal of
563 Archaeological Science 22, 211-221.
564 Pfretzschner, H.-U., 2004. Fossilization of Haversian bone in aquatic environments. Comptes
565 Rendus Palevol 3, 605-616.
566 Pickford, M., 1974. Stratigraphy and Palaeoecology of five late Cainozoic formations in the
567 Kenya Rift Valley. University of London (Unpublished PhD Thesis).
568 Pickford, M., 1978. Stratigraphy and mammalian palaeontology of the late-Miocene Lukeino
569 Formation, Kenya. In: Bishop, W.W. (Ed.), Geological Background to Fossil Man.
570 Scottish Academic Press, Edinburgh, pp. 263-278.
571 Pickford, M., Senut, B., 2001. The geological and faunal context of Late Miocene hominid
572 remains from Lukeino, Kenya. Comptes Rendus de l'Académie des Sciences de Paris-
573 Series IIA, Earth and Planetary Sciences 332, 145-152.
574 Pickford, M., Senut, B., Gommery, D., Treil, J., 2002. Bipedalism in *Orrorin tugenensis*
575 revealed by its femora. Comptes Rendus Palevol 1, 191-203.
576 Pickford, M., Senut, B., Cheboi, K., 2009. The Geology and Palaeobiology of the Tugen
577 Hills, Kenya: Rift Tectonics, Basin Formation, Volcanics and Sedimentation. Geo-Pal
578 Kenya 1, 4-133.
579 Pucéat,E., Reynard, B., Lécuyer, C., 2004. Can crystallinity be used to determine the degree
580 of chemical alteration of biogenic apatites? Chemical Geology 205, 83-97.
581 Sawada, Y., Pickford, M., Senut, B., Itaya, T., Hyodo, M., Miura, T., Kashine, C., Chujo, T.,
582 Fujii, H., 2002. The age of *Orrorin tugenensis*, an early hominid from the Tugen Hills,
583 Kenya. Comptes Rendus Palevol 1, 293-303.

584 Ségalen L., Rafélis (de) M., Lee-Thorp J.A., Maurer A-F., Renard M., 2008.
585 Cathodoluminescence tools provide clues to depositional history in Miocene and Pliocene
586 teeth, Special issue "V International Bone Diagenesis Meeting". Palaeogeography,
587 Palaeoclimatology, Palaeoecology 266, 246-253.
588 Senut, B., Pickford, M., Gommery, D., Mein, P., Cheboi, K., Coppens, Y., 2001. First
589 hominid from the Miocene (Lukeino Formation, Kenya). Comptes Rendus de l'Académie
590 des Sciences de Paris-Series IIA, Earth and Planetary Sciences 332, 137-144.
591 Senut B, Pickford M, Gommery D., 2018. Dental anatomy of the early hominid, *Orrorin*
592 *tugenensis*, from the Lukeino Formation, Tugen Hills, Kenya. Revue de Paléobiologie 37,
593 577-591. DOI: 10.5281/zenodo.2545075.
594 Tiercelin, J.-J., Lezzar, K.-E., 2002. A 300 million years history of rift lakes in Central and
595 East Africa: an updated broad review. In: Odada, E.O., Olago, D.O. (Eds.), The East
596 African Great Lakes: Limnology, Paleolimnology and Biodiversity. Advances in Global
597 Change Research 12, pp. 3 - 60.
598 Tiercelin, J.J., Vincens, A., 1987. Le Demi-graben de Baringo-Bogoria, Rift Gregory, Kenya.
599 Bulletin du Centre de Recherche et d'Exploration 11. Elf Aquitaine Production, Pau,
600 France, pp. 249-540.
601 Trueman, C.N., Behrensmeyer, A.K., Potts, R., Tuross, N., 2006. High-resolution records of
602 location and stratigraphic provenance from the rare earth element composition of fossil
603 bones. Geochimica et Cosmochimica Acta 70, 4343-4355.
604 Williams, L.A.J., Chapman, G.R., 1986. Relationships between major structures, salic
605 volcanism and sedimentation in the Kenya Rift from the equator northwards to Lake
606 Turkana. In: Frostick, L.E., Renaut, R.W., Reid, I., Tiercelin, J.-J. (Eds.), Sedimentation
607 in the African Rifts. Geological Society of London Special Publication 25, pp. 59-74.
608 .
609

610 **Table captions**

611

612 **Table 1.** Mineralogical composition of nodules, bones and enclosing clay layer (in %,
613 uncertainty ±5%); crystallinity index (CI) of the apatite calculated from XRD diffractograms
614 (without units, uncertainly ±0.02); and histological index (HI) associated, determined by
615 optical observations (without unit). See Fig. 2 for the location of samples.

616

617 **Table 2.** Chemical composition of nodules and the OS bone. See Fig. 2 for the location of
618 samples. a) Geochemical analyses of some samples from calcium phosphate nodules and
619 bone. b) SRM values used for geochemical analyses (bone ash: hydroxylapatite). **In this**
620 **study SRM is also used on reference fresh bone for comparison with the studied bone**
621 **and nodules**. c) For comparison, chemical composition of: Reference carbonate-fluorapatite
622 (francolite), specimen from Wheal Franco, Devon, England (Palache et al., 1951) and
623 Reference carbonate-hydroxylapatite, specimen from the Kaiserstuhl, Germany (Palache et
624 al., 1951). All values are in weight %. na: not analysed. (1) Calculated in this paper from the
625 bibliographic data.

626

Figure captions

Figure 1. Location map of the studied site (Aragai) within the Lukeino Formation (Tugen Hills, northwest of Lake Baringo, Kenya). The fault network represented on the map is after Pickford and Senut (2001).

Figure 2. Sedimentological data, materials studied and mineralogy of nodules and the enclosing clayey layer. (a) Synthetic lithological columns of the Lukeino Formation and the Aragai sedimentary sequence (Dericquebourg, 2016). The brown lines and the dotted line indicate the respective stratigraphic positions of the Aragai sedimentary sequence and the ARG 13 sedimentary layer containing nodules, on the lithological column of the Lukeino Formation. The stratigraphy and ages are after Sawada et al. (2002). (b) Field photo showing the nodules *in situ* within the ARG 13 sediment layer. (c) Studied material and location of different samples extracted from the four nodules (NR, NG, NM, PNR) and the altered bone (OS). (d) XRD diffractogram of the enclosing clay layer (ARG 13) and pie chart showing the mineralogical composition. S – smectite; F – K-feldspar (sanidine); Q – quartz. (e) XRD diffractogram of the NR06 sample extracted from the NR nodule and pie chart showing the mineralogical composition, which reflects the mean mineralogy of different studied nodules. S - smectite; F - K-feldspar (sanidine); A - apatite (carbonate-fluorapatite).

Figure 3. Evolution of the crystallinity index (CI) and histological index (HI) between the studied nodules and bones. CI values lower than 1 corresponding to recrystallized carbonate-hydroxylapatite and CI value higher than 1 corresponding to neoformed carbonate-fluorapatite. The location of the samples is provided in Fig. 2.

Figure 4. Ternary diagram showing similarities in chemical composition between the calcium phosphate nodules and the OS altered bone. Values of NIST SRM 1400 (bone ash: hydroxylapatite) are indicated for comparison (black star).

Figure 5. Mineralogy and internal structure of nodules. (a) Cathodoluminescence observation (NR nodule). Nodules are composed of a micritic matrix of carbonate-fluorapatite in bright yellow including feldspar (sanidine). (b) SEM image (NR nodule) showing pores in the phosphate matrix, observed only at the microscopic scale. (c) Optical microscope observation (NR nodule). The matrix of apatite contains numerous spheres of oxide (goethite and groutite); crystals in the form of needles are observed at the transition matrix - cavities.

Figure 6. Mineral neoformations inside bone cavities (OS bone). (a) SEM image (back-scattered electrons) showing the infilling of a cavity of the trabecular bone structure. (b) Optical microscope observation of the same cavity of the trabecular bone structure. (c) Interpretive drawing of this cavity of the trabecular bone structure. (d) Cathodoluminescence observation at a larger scale. The neoformation of carbonate-fluorapatite is in bright yellow. a - carbonate-hydroxylapatite, b - altered carbonate-hydroxylapatite, c - clay, d - Fe and Mn oxides, e - silica, f - carbonate-fluorapatite, g - bone porosity.

Figure 7. Transformation of bone structures with processes of dissolution-recrystallisation and precipitation leading to the formation of the calcium phosphate matrix observed in the OS bone. (a) SEM image (back-scattered electrons). (b) Interpretive drawing: a - carbonate-hydroxylapatite, b - altered carbonate-hydroxylapatite, c - clay, d - Fe and Mn oxides, e - silica, f - carbonate-fluorapatite, g - bone pores.

Figure 8. Conceptual synthesis of processes responsible for the genesis of calcium phosphate nodules from the transformation and dissolution of bone structures. Optical microscope photos were made on the KAP 07 relatively fresh bone (photos A and B), the OS altered bone (photos C to I) and the NM nodule (photo J). Legend of drawings as in Fig. 7. The blue mineral corresponds to K-feldspar (sanidine). IH: histological index. * according to Pfretzschner (2004).

684 Table 1

Sample		Smectite %	Quartz %	Sanidine %	Opal CT %	Gr-Go %	Apatite %	CI	HI
Clay layer									
ARG 13		90	4	6	-	-	-	-	-
Nodules									
NR01		3	-	5	-	-	93	0.84	0
NR02		3	-	-	-	-	97	0.86	0
NR03		-	-	-	-	-	100	0.85	0
NR04		-	-	5	-	9	87	0.87	0
NR05		-	-	8	-	-	92	0.77	0
NR06		2	-	10	-	-	88	0.81	0
NG01		3	-	8	-	-	89	0.72	0
NG02		2	-	13	12	-	73	0.82	0
NG03		4	-	10	-	-	86	0.77	0
NM01		3	-	13	-	-	84	0.71	0
NM02		7	-	12	-	8	74	0.77	0
NM03		5	-	11	-	14	70	0.83	0
NM04		4	-	14	-	-	82	0.76	0
PNR01		4	-	22	-	-	74	0.81	0
PNR02		7	-	16	-	-	77	0.88	0
Mean		*3*	-	*10*	-	-	*84*	*0.80*	*0*
Variation	Min.	0	-	0	0	0	70	0.71	0
	Max.	7	-	22	12	14	100	0.88	0
Bones									
OS01		-	-	-	-	23	77	1.03	4
OS02		7	10	13	-	-	70	1.27	0<HI<1
OS03		-	10	-	-	10	80	0.92	0<HI<1
OS04		-	-	-	-	-	100	0.62	4<HI<5
KAP07		-	-	-	-	-	100	0.41	4
Variation	Min.	0	0	0	-	0	70	0.41	0<HI<1
	Max.	7	10	13	-	23	100	1.27	4<HI<5

685

686

687 Table 2

688

Reference	Sample		P_2O_5 %	CaO %	F %	Fe_2O_3 %	MnO %	MgO %	SrO %	BaO %	SiO_2 %	Al_2O_3 %	Na_2O %	K_2O %	total %	CaO/P_2O_5	F/P_2O_5
a)																	
This study	*Nodules*																
	NM01		31.1	44.5	2.9	2.4	0.4	0.03	0.7	0.07	na	na	na	na	82.1	1.4	0.1
	NM03		30.0	42.3	2.5	4.9	0.7	0.02	0.6	0.06	na	na	na	na	81.0	1.4	0.1
	NM04		32.2	44.1	2.5	3.5	0.6	0.02	0.5	0.05	na	na	na	na	83.4	1.4	0.1
	PNR01		33.5	46.1	2.9	2.3	0.3	0.01	0.6	0.03	na	na	na	na	85.7	1.4	0.1
	Mean		*31.7*	*44.3*	*2.7*	*3.3*	*0.5*	*0.02*	*0.6*	*0.05*	*na*	*na*	*na*	*na*	*83.0*	*1.4*	*0.1*
	Variation	Min.	30.0	42.3	2.5	2.3	0.3	0.01	0.5	0.03	na	na	na	na	81.0	1.4	0.1
		Max.	33.5	46.1	2.9	4.9	0.7	0.03	0.7	0.07	na	na	na	na	85.7	1.4	0.1
	Bone																
	OS01		32.5	44.1	2.6	1.6	0.2	0.01	0.3	0.03	na	na	na	na	81.4	1.4	0.1
	OS02		33.9	43.5	2.1	2.3	0.4	0.01	0.3	0.03	na	na	na	na	82.5	1.3	0.1
	OS04		34.9	47.7	2.9	1.2	0.2	0.02	0.3	0.04	na	na	na	na	87.2	1.4	0.1
	Mean		*33.8*	*45.1*	*2.5*	*1.7*	*0.3*	*0.01*	*0.3*	*0.03*	*na*	*na*	*na*	*na*	*83.7*	*1.4*	*0.1*
	Variation	Min.	32.5	43.5	2.1	1.2	0.2	0.01	0.3	0.03	na	na	na	na	81.4	1.3	0.1
		Max.	34.9	47.7	2.9	2.3	0.4	0.02	0.3	0.04	na	na	na	na	87.2	1.4	0.1
b)																	
This study	SRM (bone ash)		40.8	51.7	0.1	0.04	0.003	1.04	0.03	0.03	na	na	na	na	93.8	1.3	0.003
Manufacturer data	SRM (bone ash)		41.1	53.5	0.1	0.09	0.002	1.14	0.03	-	0.3	0.1	0.81	0.02	97.2	1.3	0.003
Laboratory	*SRM mean (long-term)*		*42.3*	*52.8*	*0.1*	*0.04*	*0.002*	-	*0.03*	*0.03*	-	-	-	-	*95.4*	*1.2*	*0.003*
	Number of analyses		3	10	3	5	7		8	11							
c)																	
Palache et al., 1951	Carbonate-fluorapatite		38.13	53.94	3.71	0.34	-	0.1	-	-	-	-	-	-	-	1.4[(1)]	0.1[(1)]
Palache et al., 1951	Carbonate-hydroxylapatite		38.7	51.8	0.93	-	-	-	0.32	-	1.13	-	-	-	-	1.3[(1)]	0.02[(1)]

689

690 Figure 1

691

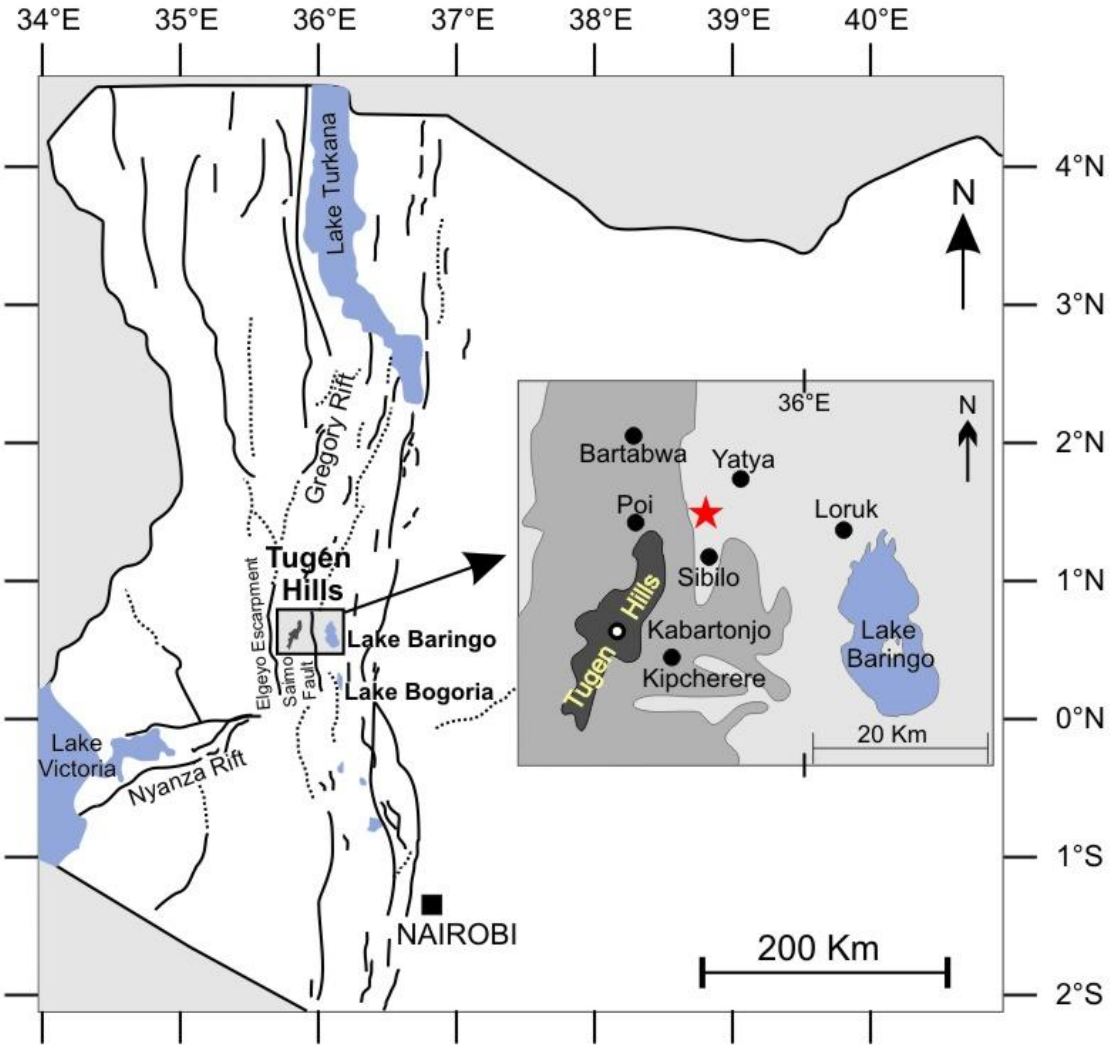

692

693

694 Figure 2

695

696

697

698

699

700

701

702

703

704

705

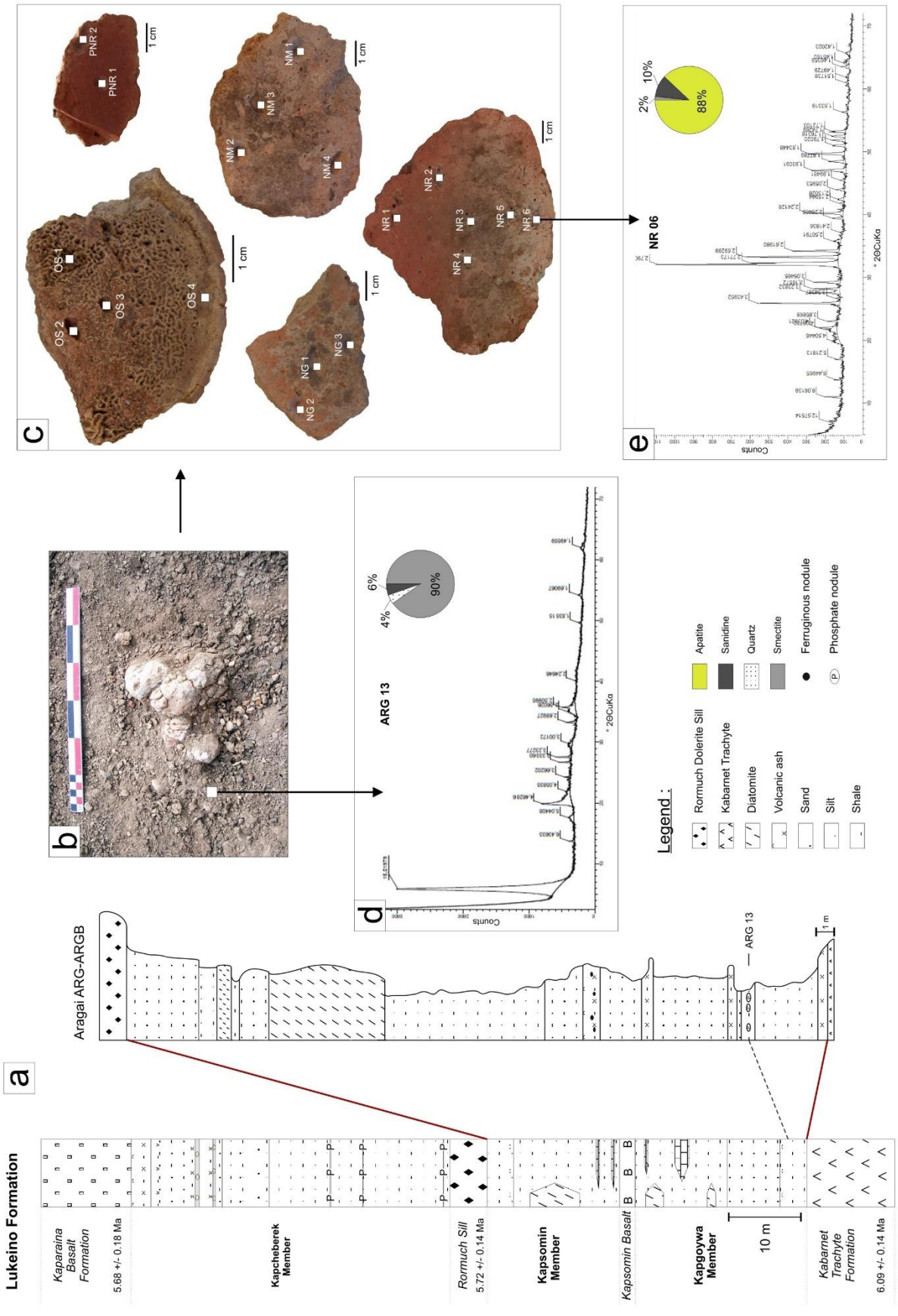
a
Lukeino Formation
Kaparaina Basalt Formation
5.68 +/- 0.18 Ma
Kapcheberek Member
Rormuch Sill
5.72 +/- 0.14 Ma
Kapsomin Member
Kapsomin Basalt
Kapgoywa Member
10 m
Kabarnet Trachyte Formation
6.09 +/- 0.14 Ma
Aragai ARG-ARGB
ARG 13
1 m
b
c
OS 1
OS 2
OS 3
OS 4
NG 1
NG 2
NG 3
NM 1
NM 2
NM 3
NM 4
PNR 1
PNR 2
NR 1
NR 2
NR 3
NR 4
NR 5
NR 6
1 cm
d
ARG 13
6%
4%
90%
Counts
° 2θCuKα
e
NR 06
2%
10%
88%
Counts
° 2θCuKα
Legend :
Rormuch Dolerite Sill
Kabarnet Trachyte
Diatomite
Volcanic ash
Sand
Silt
Shale
Apatite
Sanidine
Quartz
Smectite
Ferruginous nodule
Phosphate nodule

706

707 Figure 3

708

709

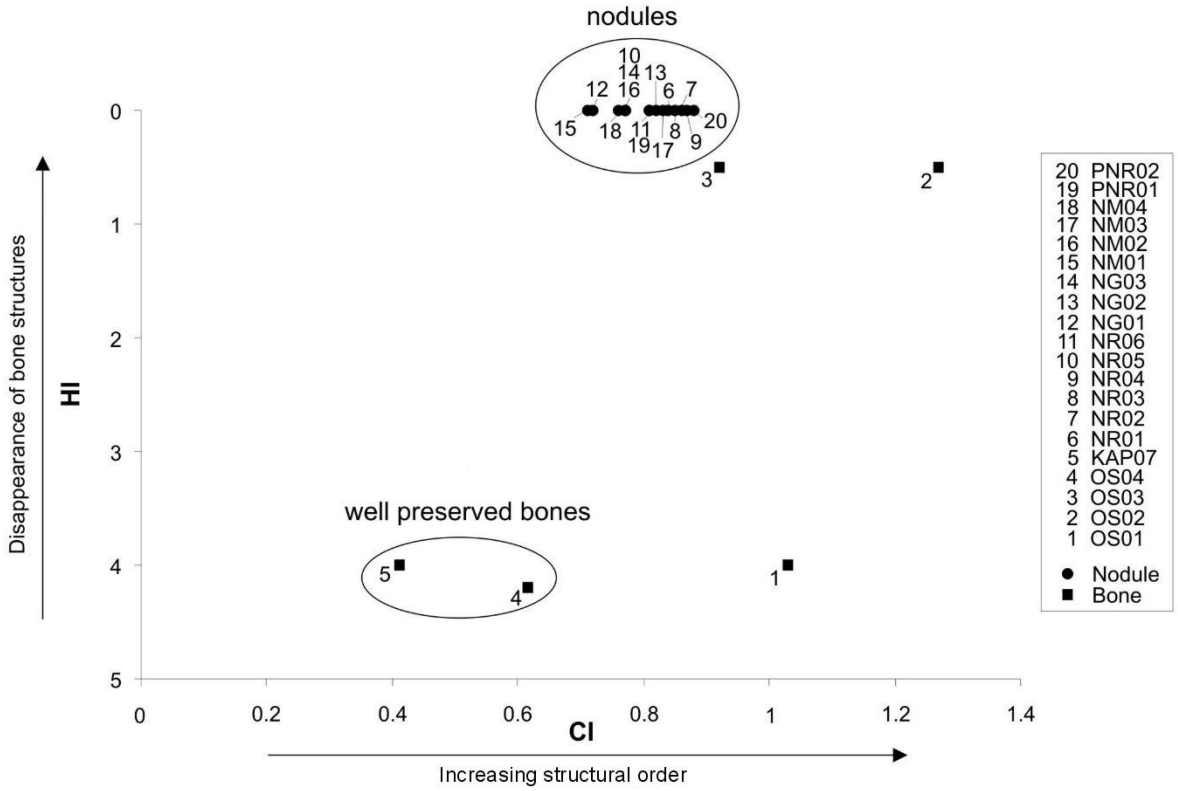

710

711

712

713 Figure 4

714

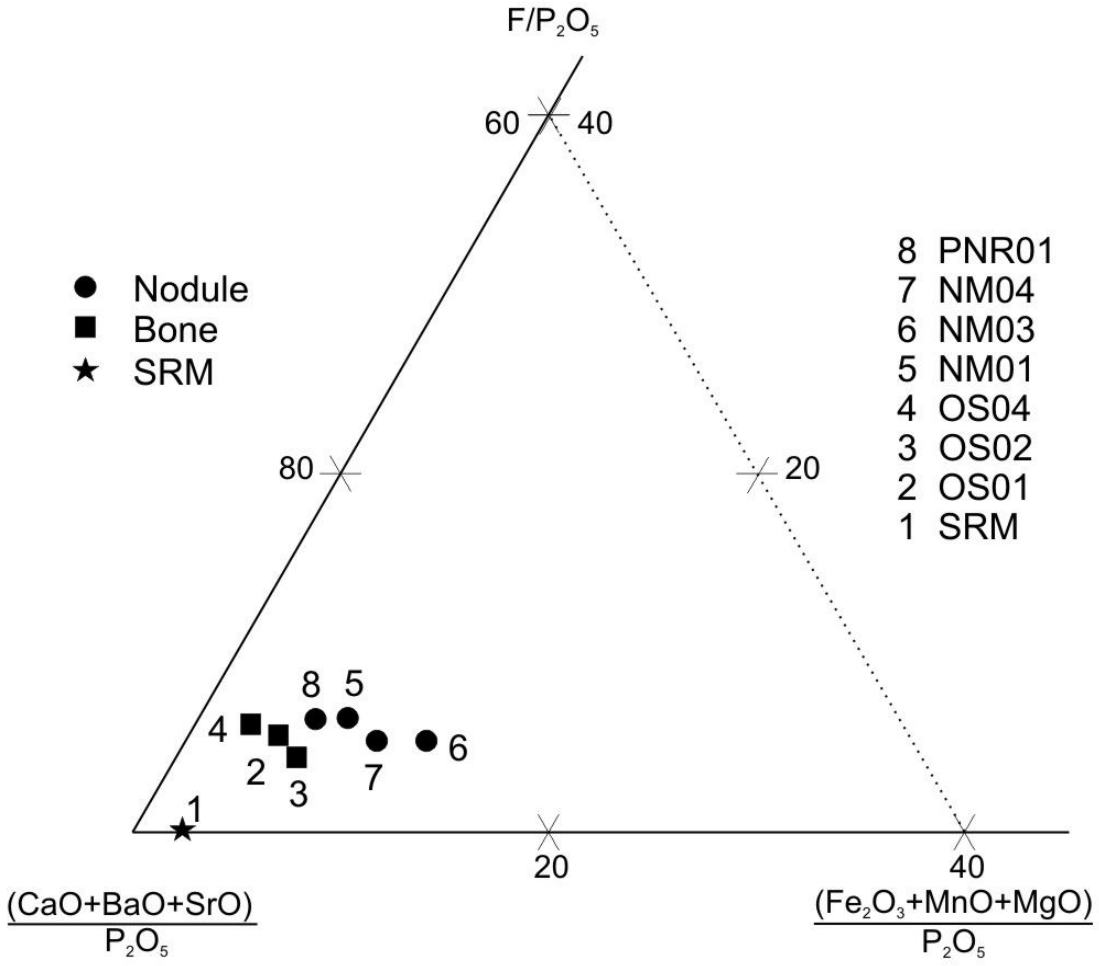

715

716 Figure 5

717

718

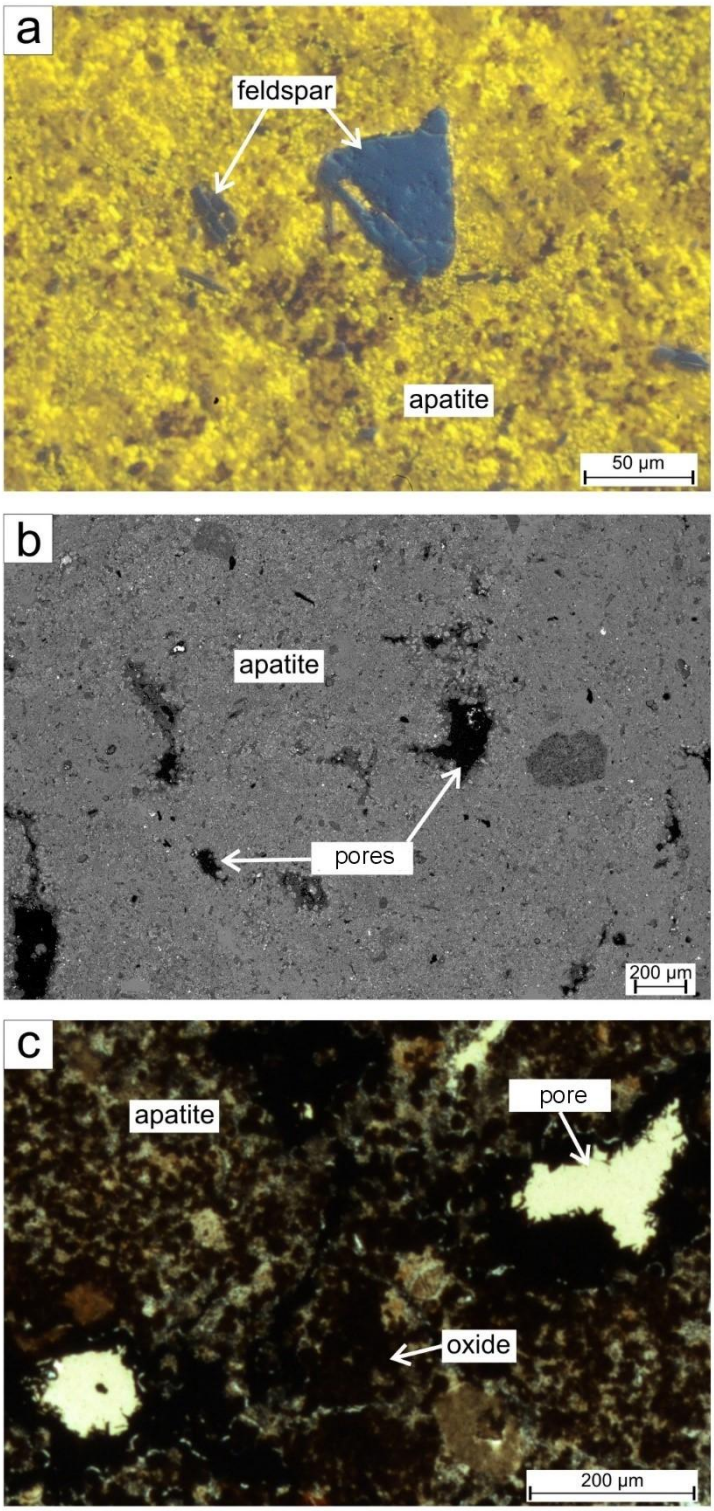

719

720 Figure 6

721

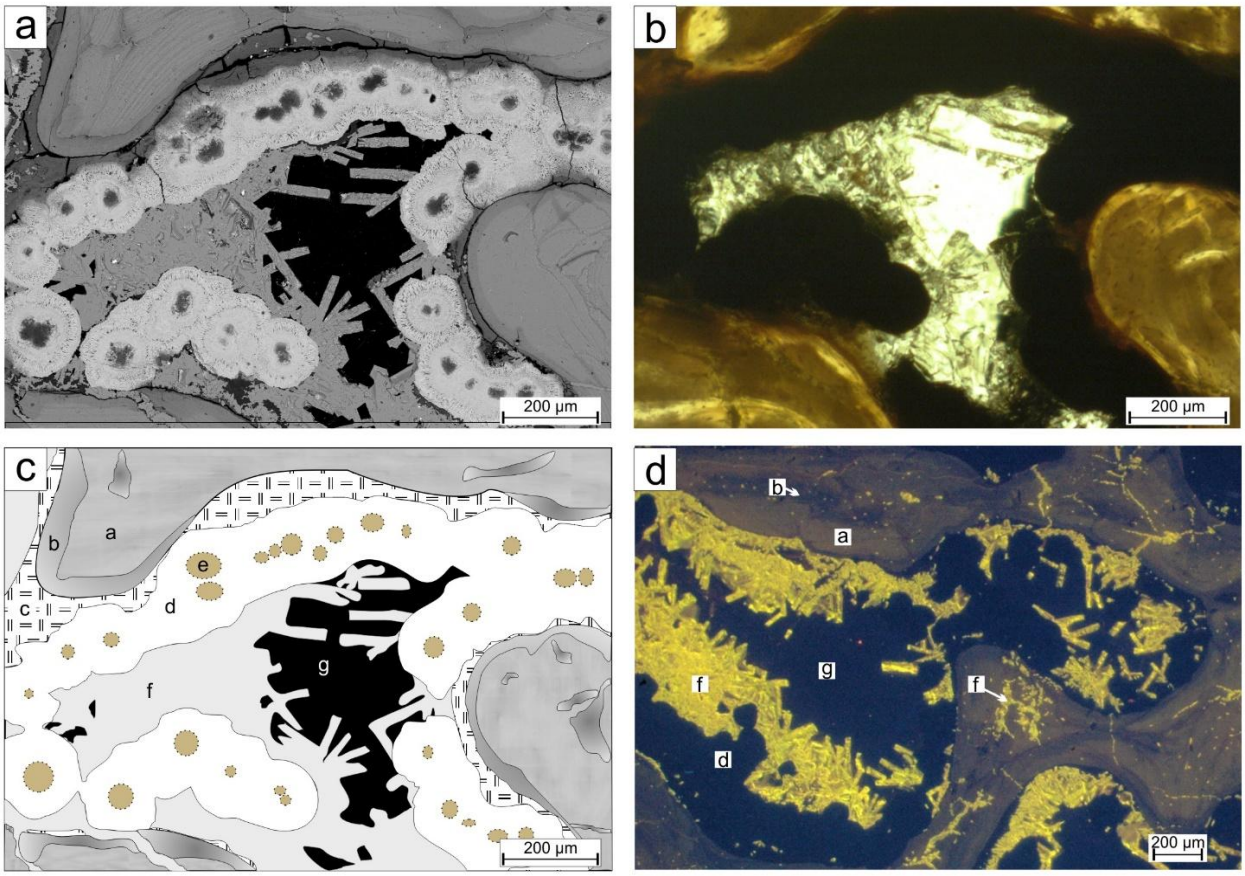

722

723 Figure 7

724

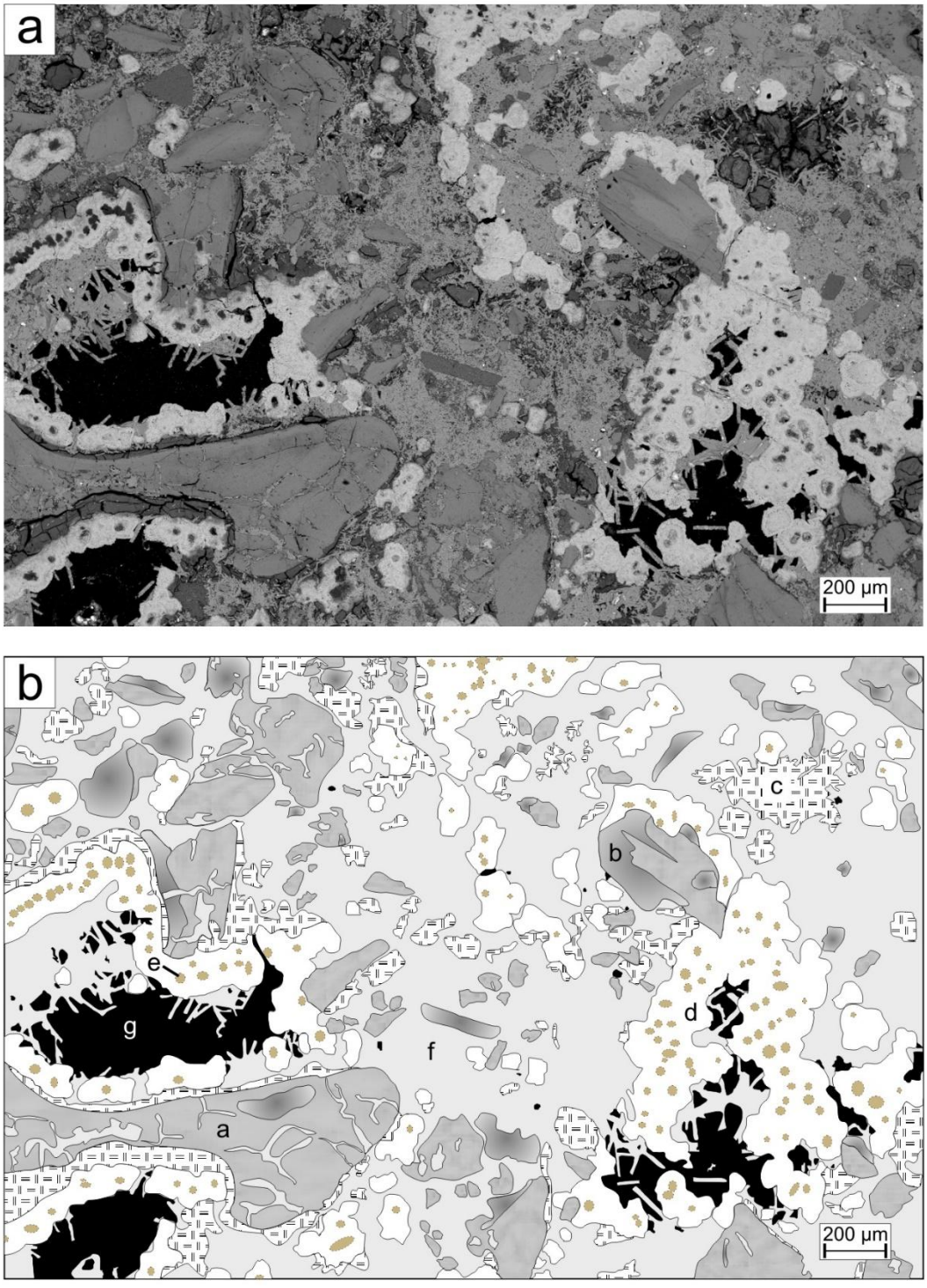

725

726 Figure 8

727

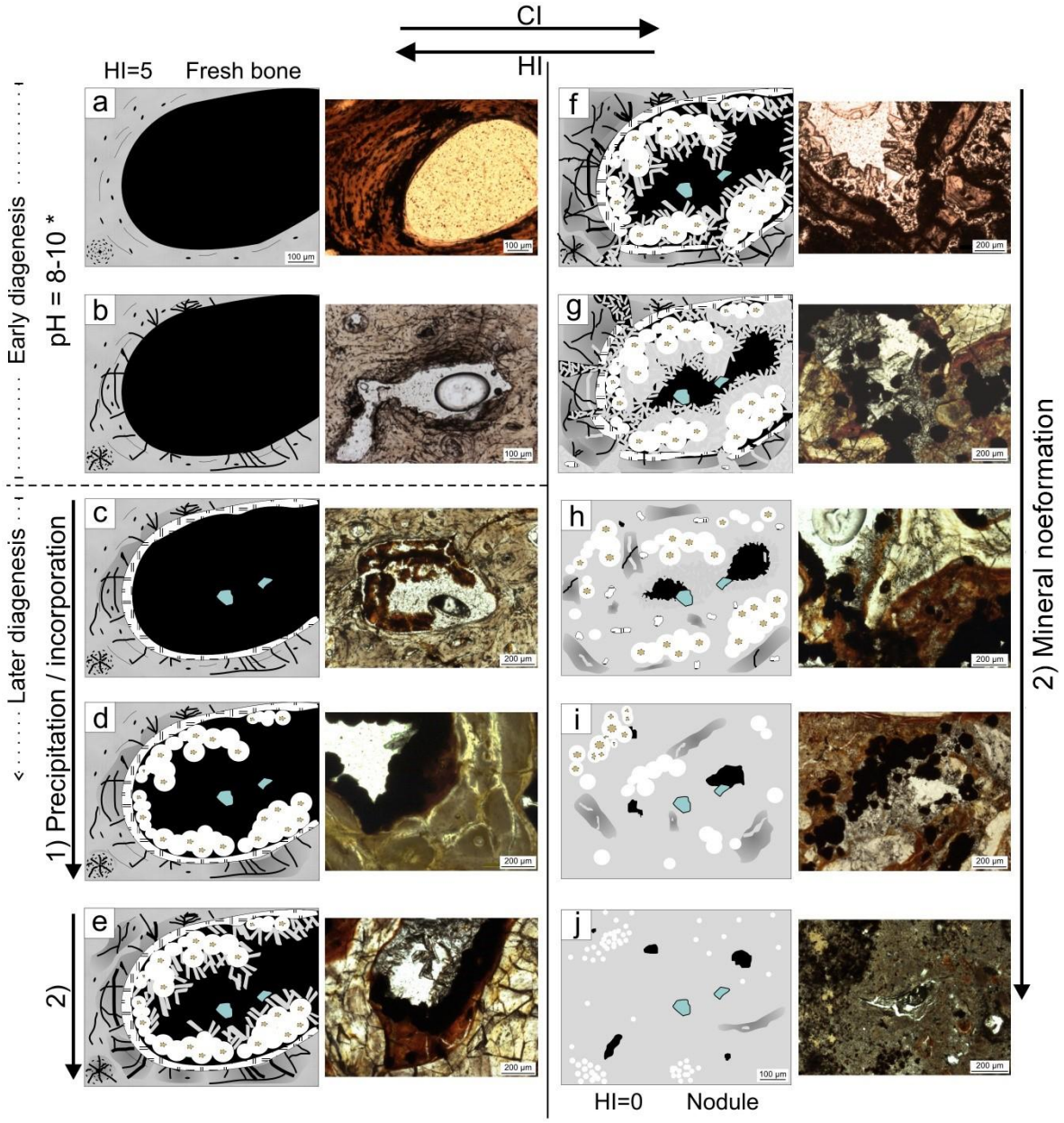

728